Article

Slope Superficial Displacement Monitoring by Small Baseline SAR Interferometry Using Data from L-band ALOS PALSAR and X-band TerraSAR: A Case Study of Hong Kong, China

Fulong Chen [1,2,*], Hui Lin [3,4] and Xianzhi Hu [3]

[1] Key Laboratory of Digital Earth Science, Institute of Remote Sensing and Digital Earth, Chinese Academy of Sciences, No. 9 Dengzhuang South Road, Haidian District, Beijing 100094, China

[2] International Centre on Space Technologies for Natural and Cultural Heritage under the Auspices of UNESCO, No. 9 Dengzhuang South Road, Haidian District, Beijing 100094, China

[3] Institute of Space and Earth Information Science, The Chinese University of Hong Kong, ShaTin, Hong Kong 999077, China; E-Mails: huilin@cuhk.edu.hk (H.L.); huxianzhi@cuhk.edu.hk (X.H.)

[4] Department of Geography and Resource Management, The Chinese University of Hong Kong, ShaTin, Hong Kong 999077, China

* Author to whom correspondence should be addressed; E-Mail: chenfl@radi.ac.cn; Tel.: +86-10-8217-8198; Fax: +86-10-8217-8915.

Abstract: Owing to the development of spaceborne synthetic aperture radar (SAR) platforms, and in particular the increase in the availability of multi-source (multi-band and multi-resolution) data, it is now feasible to design a surface displacement monitoring application using multi-temporal SAR interferometry (MT-InSAR). Landslides have high socio-economic impacts in many countries because of potential geo-hazards and heavy casualties. In this study, taking into account the merits of ALOS PALSAR (L-band, good coherence preservation) and TerraSAR (X-band, high resolution and short revisit times) data, we applied an improved small baseline InSAR (SB-InSAR) with 3-D phase unwrapping approach, to monitor slope superficial displacement in Hong Kong, China, a mountainous subtropical zone city influenced by over-urbanization and heavy monsoonal rains. Results revealed that the synergistic use of PALSAR and TerraSAR data produces different outcomes in relation to data reliability and spatial-temporal resolution, and hence could be of significant value for a comprehensive understanding and monitoring of unstable slopes.

1. Introduction

A landslide (resulting from slope instability) is the movement of a mass of rock, debris, or earth down a slope under the influence of gravity [1], threatening infrastructures, residential zones, and cultural heritage sites. Therefore, it has been regarded as one of the most problematic natural hazards in many countries due to the high-levels of socio-economic damage it inflicts on impacted regions [2]. Causes of landslide are many; however, they can be divided into two categories. The first include environmental factors, namely terrain, slope gradients, geological and soil conditions, geomorphology, land use and land cover. They are intrinsic elements of landslide prediction models. The second category refers to external triggering factors, such as intense rainfall, earthquake or anthropogenic activities. Information on these external triggering factors generally has more temporal than spatial importance [3]. Landslides can involve flowing, sliding, toppling or falling, determined by a combination of two or more causal elements belonging to one or a combination of the two categories mentioned above.

Slope superficial displacement is one of the most significant pre-cursors of landslides, and thus the kinematics monitoring before hazards or even after an event is increasingly imperative for policymakers and emergency managers. As a complementary tool for conventional surveying, remote sensing offers a synoptic view for landslide characterization and prediction [4,5]. Unlike optical remote sensing (that detects changes in spectral signatures), differential synthetic aperture radar interferometry (DInSAR), particularly the multi-temporal SAR interferometry (MT-InSAR), has proved to be effective for surface motion detection and time series analysis (e.g., for phenomena ranging from landslides to tectonics, earthquakes, glacier evolution, volcanism and anthropogenic processes) [6–12]. MT-InSAR measures the phase difference of two or multi-temporal SAR acquisitions and can be divided into two categories: persistent scatterer (PS) SAR interferometry (PS-InSAR) [13–15] and small baseline SAR interferometry (SB-InSAR) [16–19]. The former identifies pixels primarily on phase variation in time or phase correlation in space, corresponding to point-like targets or so-called PS points (e.g., man-made structures, boulders and outcrops), and the full resolution can be preserved. The phase decorrelation of those point-targets, considered to be dominant scatterers, is minimal even with large temporal and geometric baselines. The latter refers to the small baseline interferometric formation primarily dealing with distributed scatterers (DSs). DSs share the same statistical behavior within a spatial extent, and can be represented by debris areas and non-cultivated land. Multi-looking and interferogram filtering are preferred for the purpose of signal-to-clutter ratio enhancement at the expense of spatial resolution loss. More recently, innovative methods have been developed for synergistically using PS and DS to increase the density of detected targets [20,21].

In general, MT-InSAR can be used to determine the art of surface motion evolution for individual landslides, or to identify unstable areas that have not been previously detected [22–30]. However,
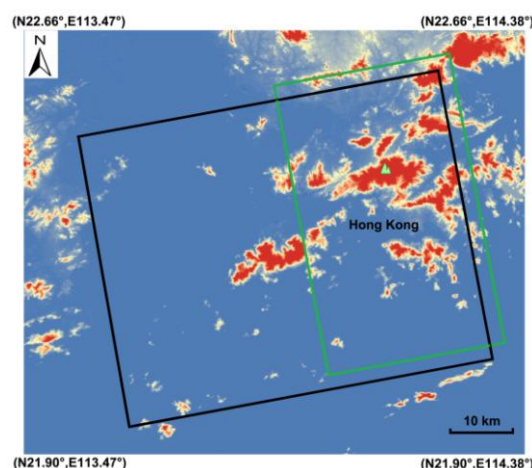
investigations using MT-InSAR are still inadequate with regard to the following: (1) the density of PSs is too sparse to discriminate the boundaries of unstable areas because only point-like targets are identified; (2) only single-band SAR images have been utilized even though multi-band data are available; (3) studies using data from the newly launched high-resolution SAR data, such as TerraSAR-X [31] or the constellation of Cosmo-SkyMed [32], are rare and need further exploitation.

In this study, we used an improved SB-InSAR method to monitor the slope superficial displacement in Hong Kong, China. Hong Kong's mountainous terrain, heavy rainfall and dense development expose local residents to risk from landslides [33]. Taking advantage of characteristics of the two different spaceborne SAR data (high coherence preservation of ALOS PALSAR, high resolution and short revisit cycle of TerraSAR-X), an improvement of the detection and estimation of unstable slopes was obtained. The joint use of SAR data from two different SAR platforms with different characteristics offers different performances in terms of data reliability and spatial-temporal resolution. First, the detection capability is enhanced by means of a combined analysis of X- and L-band SAR data. Second, merits of the two different SAR systems, large spatial coverage of ALOS PALSAR and detailed information extraction of TerraSAR-X, are integrated enabling a comprehensive understanding and monitoring of unstable slopes.

2. Study Site and Geological Setting

Hong Kong (located at the Pearl River Delta, China) is approximately 1,000 square kilometers with natural terrain covering about 680 km^2, of which more than 65% have slopes greater than 15° and 30% greater than 30°, respectively. The elevation ranges approximately from 0 to 950 m with the highest peak at Tai Mo Shan at 957 m a.s.l. (marked by the light-green mountain symbol in Figure 1). Subtropical and monsoonal climate with hot and humid summers but mild and dry winters are the norm. The mean annual rainfall reaches about 2,400 mm, approximately 80% of which falls during the rainy season from May to September [34]. Rainfall is heavy and occasionally intense during rainstorms and typhoons in the summer season. The average temperature at Hong Kong is around 22.8 °C.

Figure 1. Coverage of ALOS PALSAR (marked by the black box) and TerraSAR-X data (marked by the green box) in Hong Kong, indicating the former has larger swath than the latter. Background is the SRTM DEM-shaded image, and Tai Mo Shan is marked by the light green mountain symbol.

The geology of Hong Kong has been well documented by the Civil Engineering and Development Department (CEDD) of the Hong Kong government. The majority of the land area comprises Mesozoic plutonic and volcanic rocks with the remaining area underlain by sedimentary rocks of Devonian to Tertiary age. Much of the present-day landscape of Hong Kong is assumed to have been formed during the Quaternary [35]. However, this area may have suffered from subtropical weathering as early as Tertiary, resulting in the decomposition of rock and the formation of a thick saprolite. The mountainous terrain, rock weathered covering layer, and heavy rainfall together with intense urban development jointly determine the frequent occurrence of landslides. Generally, terrain landslides are triggered by the transient perched water table at geological interfaces of the colluvium/residual soils during or after periods of intense rainfall. A total of 26,780 landslides have been reported on natural hill slopes during the 50 years from 1945 to 1994, with an average landslide frequency of more than 300 per year [36]. In general, most slope failures in Hong Kong are represented by shallow, highly disruptive and fast movements [37]; thus instead of landslides, in this study we only focus on the slope superficial displacement related to post-failures or landslide reactivation using MT-InSAR technologies. Vulnerable slope detection is significant for identifying hot-spots before potential geo-hazard events occur.

3. Available SAR and DEM Data

The following sets of multi-source spaceborne SAR data were obtained for Hong Kong: 21 scenes of L-band ALOS PALSAR data comprising 9 images in Fine Beam Single-polarization (FBS) mode with HH polarization and 12 images in Fine Beam Dual-polarization (FBD) mode with HH- and HV polarization for the period from 24 June 2007 to 2 January 2011; 43 scenes X-band TerraSAR data with Stripmap mode (VV polarization) for the period from 13 May 2008 to 26 December 2010. These data were employed in slope superficial displacement monitoring in the Hong Kong study site (see Tables 1 and 2 for details). The PALSAR data were collected with a nominal radar look angle of about 34.3 ° along the ascending orbits. For FBS data, the pixel spacing is 4.68 m in the range direction and 3.17 m in the azimuth direction compared to 9.36 m by 3.17 m in FBD mode. The TerraSAR data were collected with a nominal radar look angle of approximately 37.4 ° along the ascending orbits. The pixel spacing is 0.91 m by 2.04 m in the range and azimuth direction, respectively.

Table 1. ALOS PALSAR data used in this study covering Hong Kong, China; the image acquired in 29 June 2009 was selected as the reference for the dataset co-registration.

Acquisition Time	Polarization	Perpendicular Baseline (m)	Temporal Baseline (days)
20070624	HH/HV	2,592.75	−736
20070809	HH/HV	2,689.86	−690
20071225	HH	2,621.81	−552
20080209	HH	2,818.71	−506
20080511	HH/HV	3,303.44	−414
20080626	HH	2,811.50	−368
20080926	HH/HV	−2,934.69	−276
20081111	HH/HV	−2,558.41	−230
20081227	HH	−2,635.86	−184

Table 1. *Cont.*

Acquisition Time	Polarization	Perpendicular Baseline (m)	Temporal Baseline (days)
20090211	HH	−381.09	−138
20090629	HH/HV	0	0
20090814	HH/HV	−155.75	46
20090929	HH/HV	182.99	92
20091114	HH	324.77	138
20091230	HH	611.42	184
20100214	HH	952.09	230
20100517	HH/HV	1,074.14	322
20100702	HH/HV	1,347.14	368
20101002	HH/HV	1,639.99	460
20101117	HH/HV	1,203.67	506
20110102	HH	1,733	552

Table 2. TerraSAR-X (Stripmap) data used in this study covering Hong Kong, China; the image acquired in 14 November 2009 was selected as the reference for the dataset co-registration.

Acquisition Time	Perpendicular Baseline (m)	Temporal Baseline (days)	Acquisition Time	Perpendicular Baseline (m)	Temporal Baseline (days)
20080513	−204.08	−550	20091023	−45.16	−22
20081025	−201.70	−385	20091103	−150.58	−11
20081105	101.23	−374	20091114	0	0
20081116	−28.73	−363	20091125	−125.12	11
20081127	−141.03	−352	20091206	−138.60	22
20090110	21.92	−308	20091217	−37.91	33
20090121	−46.65	−297	20100406	−32.09	143
20090201	−123.71	−286	20100611	−32.41	209
20090212	105.68	−275	20100622	32.23	220
20090223	−179.27	−264	20100703	92.21	231
20090306	−96.90	−253	20100714	32.47	242
20090317	9.05	−242	20100725	182.34	253
20090430	9.64	−198	20100805	−138.46	264
20090511	−18.08	−187	20100816	−105.65	275
20090522	−23.53	−176	20100907	−70.67	297
20090602	−55.84	−165	20100918	−239.08	308
20090624	180.15	−143	20100929	94.53	319
20090705	60.57	−132	20101010	27.25	330
20090716	−88.08	−121	20101101	55.42	352
20090727	−46.62	−110	20101112	−79.32	363
20091001	67.76	−44	20101226	−59.14	407
20091012	−185.64	−33			

PALSAR has a longer wavelength (L-band, 23.6 cm), and hence a better vegetation penetration and coherence preservation than X-band TerraSAR (3.0 cm). In addition, the swath of PALSAR in this study is 70 km by 60 km, larger than the 30 km by 50 km swath of TerraSAR (Figure 1). TerraSAR provides spatial resolution one order of magnitude better than PALSAR and is also characterized by a

shorter revisit cycle (11 days compared to 46 days of PALSAR). These combinations of data characteristics resulted in detailed scale and better temporal resolution for ground/slope displacement assessment.

The 1:25,000-scale DEM map of Hong Kong (2.5 m by 2.5 m resolution in plane coordinates, and 5 m accuracy in vertical direction) was firstly provided as an auxiliary data for time-series SAR image co-registration. This was necessary particularly for the high resolution X-band SAR data. In general, 1/8 pixel co-registration accuracy was required to avoid significant loss of interferometric phase coherence in the interferogram generation [38]. In case of rough topography and long baseline, standard co-registration methods based on 2-D polynomial warp functions become inaccurate leading to local misregistrations; these defects increase with the spatial resolution of the data [32,39]. Therefore, the DEM-assisted image co-registration method was adopted. To minimize the signature change of observed scene due to temporal and geometric baselines, the image acquired in 29 June 2009 and the image acquired in 14 November 2009 were selected as reference images for the PALSAR and TerraSAR datasets, respectively. Then the DEM data were used for topographic phase estimation and mitigation in DInSAR procedures, and for InSAR products geocoding (transforming from SAR imaging coordinates into geographic coordinates).

4. Small Baseline InSAR (SB-InSAR) with 3-D Phase Unwrapping

The main advantage of SB-InSAR [16,18] is its capability for deformation mapping on natural scenarios where DSs are prevalent. However, spatial phase unwrapping on individual differential interferograms remains problematic, in particular when low-coherence interferograms are encountered. This drawback was overcome by an improved SB-InSAR approach with 3-D phase unwrapping (3 dimensions, including 2-D in spatial and 1-D in temporal domains, respectively). The reliability of unwrapped phase signatures in interferograms was enhanced due to the temporal constraint in unwrapping procedures.

For a set of $N + 1$ co-registered single look complex (SLC) SAR images (acquired from t_0 to t_N), procedures of SB-InSAR with 3-D phase unwrapping are as follows:
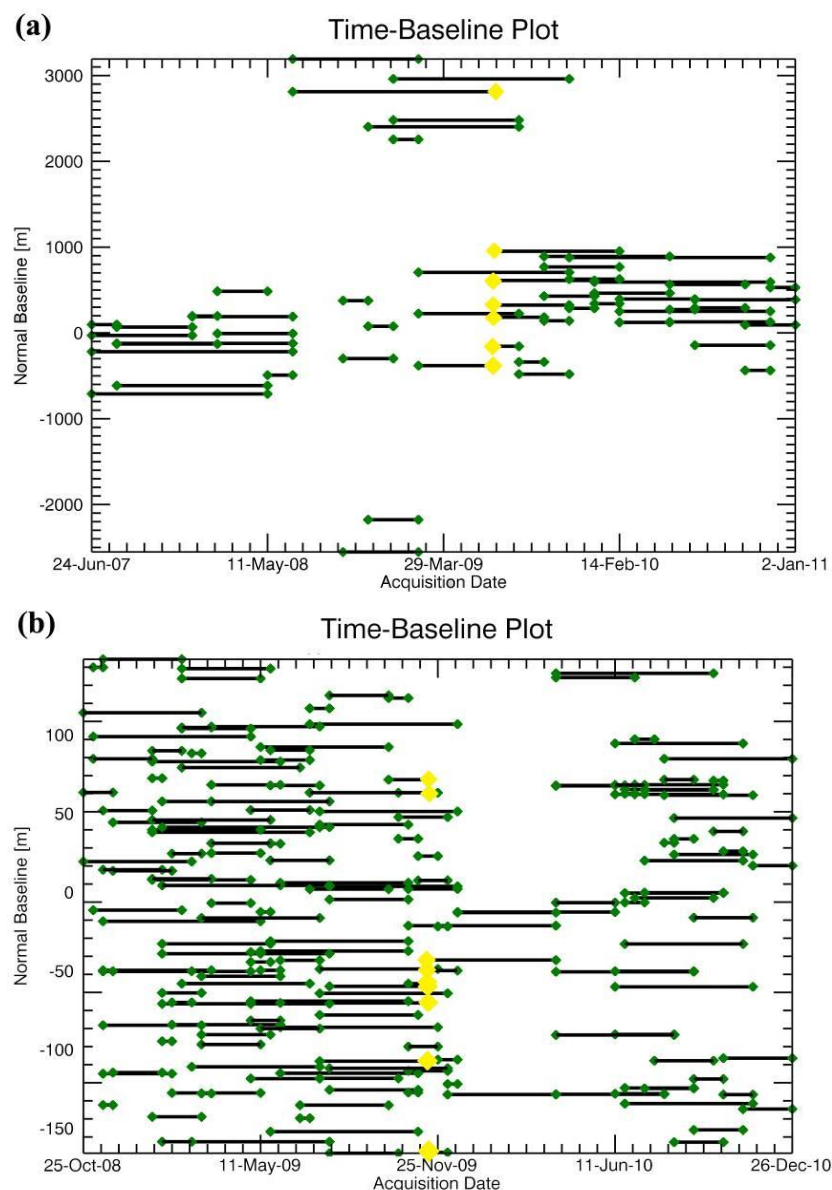
(1) The generation of M multi-looked, filtered small baseline differential interferograms (after the flat and topographic phase removal). For the ALOS PALSAR data, two thresholds for baselines (smaller than 3,000 m spatially and 368 days temporally) were first applied to generate initial interferograms; then interferograms with perpendicular baselines larger than 1,500 m were kept only if they were needed to guarantee connectivity of the subsets in time. A total of 57 final interferograms (Figure 2a) were generated. For the TerraSAR-X data, a small baseline constraint (less than 150 m spatially and 180 days temporally) was applied to generate 226 initial interferograms; of these 45 low-quality inteferograms were discarded and the remaining 181 were retained (Figure 2b). Therefore, problems of temporal and geometric decorrelation and residual phase due to uncompensated topography were mitigated. Such a baseline constraint leads to several independent interferogram subsets, and thus SB-InSAR is also termed within the scientific community as small baseline subsets (SBAS).

(2) Absolute phase estimation by means of interferogram unwrapping. Phase unwrapping is a crucial step for the successful implementation of SB-InSAR. In general, the 2-D spatial phase unwrapping is a traditional way, whether for an entire interferogram or for sparse point-targets on an interferogram [40]. Recent advances have focused on algorithms that incorporate both the temporal

and spatial dimensions, so-called 3-D phase unwrapping [41–43]. Considering the redundant network of interferograms in time, the Delauney-based 3-D phase unwrapping method [44] was applied; phase unwrapping in the spatial domain was constrained through the consistency of the network in time (see Figure 3). Note that two original TerraSAR images acquired in 13 May 2008 and 18 September 2010 were discarded during interferogram formation because of the applied spatial baseline constraint of 150 m.
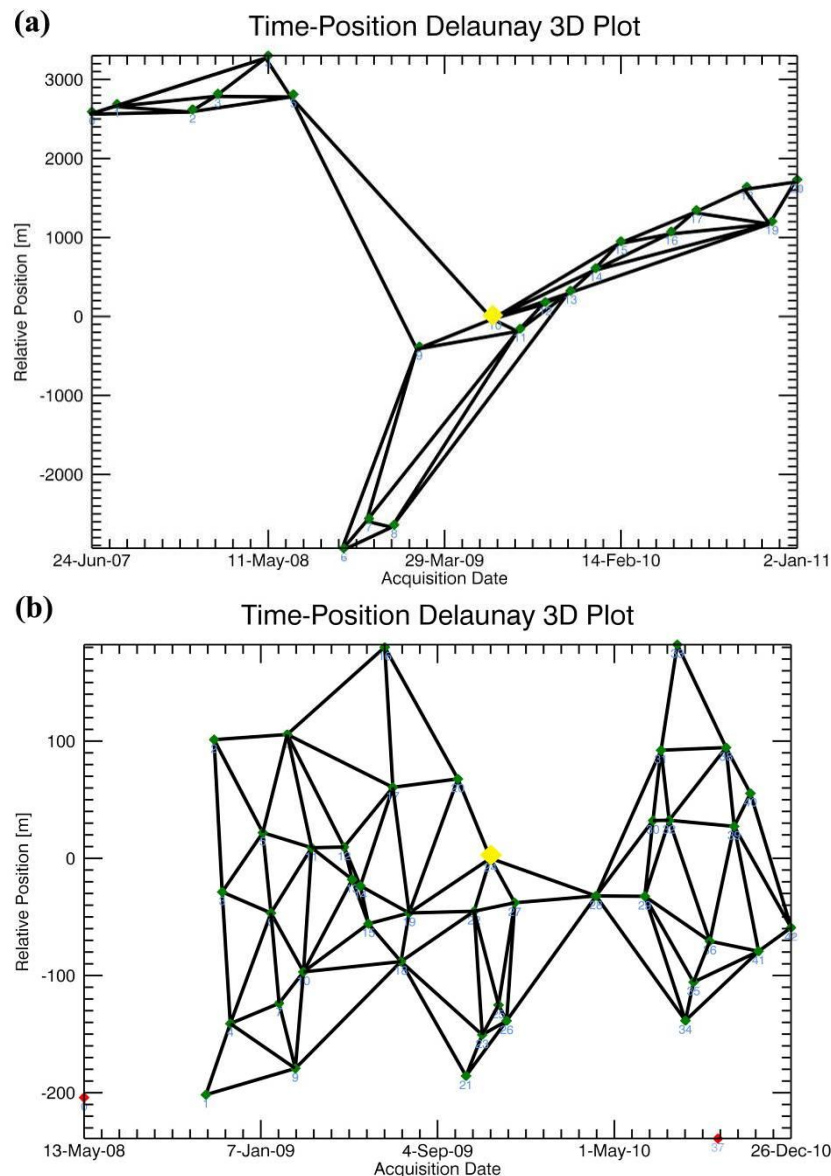
(3) A set of coherent pixels (CPs, dominated by DSs) in *M* interferograms was selected as characterized by a high coherence in the majority of total interferograms. The surface deformation time series of the selected CPs can be retrieved by singular value decomposition (SVD) as long as those subsets overlapped in time. The first step of SB-InSAR was the estimation of low-pass displacement and residual height using a preferred cubic displacement model. Then the second step was concentrated on the displacement time series retrieval and atmospheric artifact isolation. For more details, interested readers can refer to Berardino *et al.* [16].

Figure 2. Small baseline formation, (**a**) ALOS PALSAR; (**b**) TerraSAR. Yellow points indicate the reference imagery for temporal image co-registration.

Figure 3. Estimated Delauney network of interferograms in spatial and temporal domain, (**a**) ALOS PALSAR; (**b**) TerraSAR. The yellow point indicates the reference imagery for temporal image co-registration; and red points in (b) indicate two TerraSAR images discarded due to the spatial baseline threshold (150 m).
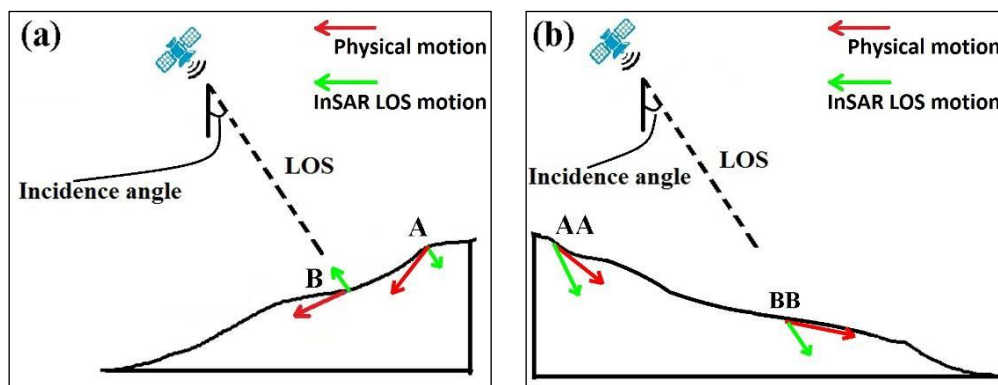

5. Results and Interpretation

As we know, InSAR techniques only measure the surface deformation in the direction of line of sight (LOS). Owing to the small incidence angle of sensors, land settlements in flat terrain (e.g., cities) can be seen as subsiding when the vertical motion is dominant (caused by mining or underground water overexploitation). However, this is not true for slope monitoring. In general, the motion mechanism of slopes primarily consists of translational and rotational motion. Here we assumed that a hypothetical rotational or compound slide that leads to a progressive flattening of the vectors from the upper part (where vectors are almost vertical) to the lower part (where vectors are almost horizontal) of the slope (see Figure 4). The slopes facing the sensors show mild LOS subsidence in upper section with steep terrain (the slope gradient > incidence angle, marked by "A"), and mild LOS uplift in

median-lower slope section (the slope gradient < incidence angle, marked by "B"), respectively. For the backslope, the corresponding motions demonstrate as moderate-mild LOS subsidence (marked by "AA" and "BB"). Thereby, both the subsidence and uplift with significant LOS InSAR values can be determined for suspected unstable slopes and can be further analyzed jointly using additional topography data (e.g., slope gradients, layover and shadow).

Figure 4. Geometric relationship between SAR incidence angle (ascending path) and slope physical motion trends; (**a**) slope facing the sensor demonstrates as mild LOS subsidence ("A") or LOS uplift ("B"); (**b**) slope facing away from the sensor demonstrates as moderate ("AA") to mild ("BB") LOS subsidence.
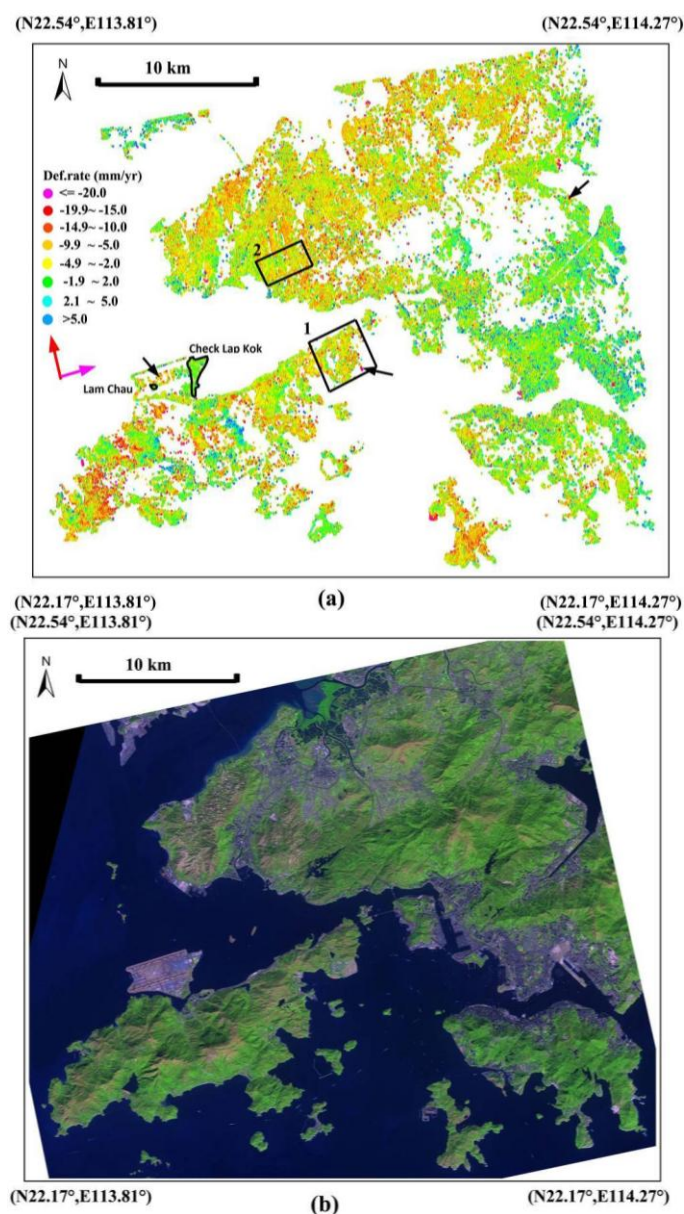

5.1. ALOS PALSAR

There are two kinds of ALOS PALSAR data in Fine mode: FBS (range bandwidth of 28 MHz) and FBD (14 MHz). The range bands are fully overlapped due to the same center frequency, permitting interferometric processing of mixed FBS-FBD pairs with common HH polarization (FBD data needed to be doubly oversampled in the range direction). In this study, a subset of the region covering Hong Kong was spatially cropped from the whole scene for slope superficial motion surveillance. Due to the corrective satellite orbit manoeuvre [45], the small baseline interferograms turned into several clusters, implying the feasibility of the SB-InSAR method for surface motion inversion. 5×2 multi-looking (azimuth by range) and the Goldstein filter [46] were applied during the interferogram generation, resulting in approximately 16 m ground resolution of InSAR products. The PALSAR-derived surface motion in LOS direction over Hong Kong is illustrated in Figure 5a. The corresponding values were primarily in the range of −20 mm/yr to 5 mm/yr for the 3.5 yr observation period. Negative motion rates indicate increasing distance with time or motion away from the satellite (consistent with subsidence); and positive rates are consistent with uplift. As a preliminary quantitative validation, the leveling data covering Hong Kong International Airport (HKIA) were used. Except for the original Check Lap Kok Island and Lam Chau Island, marked by polygons in Figure 5a, other reclamation sections in HKIA demonstrated mild ground subsidence (in the range of −14 mm/yr to −5 mm/yr), in agreement with the ground-based leveling data. A large number of CPs (752,648) were detected, *i.e.*, 376 CPs/km^2 in an area of approximately 50×40 km^2. It is clear that an abundance of CPs was located in vegetated slopes (see Figure 5b), implying the potential of SB-InSAR for slope susceptibility monitoring using ALOS PALSAR data (for more quantitative evaluation, see Section 5.3).

Apart from the reclamation lands (marked by the black arrows in Figure 5a, showing areas of settlements), a portion of the mountainous region, e.g., Lantau Island, western and northwestern parts of New Territories, was unstable with LOS values larger than ±2.0 mm/yr (an appropriate threshold closing to the measurement sensitivity of the SB-InSAR approach, which discriminates moving from nonmoving targets). The SB-InSAR derived signature confirmed that the natural slopes over Hong Kong were unstable jointly as a result of the environmental conditions (e.g., loosely compacted rock-weathered mantle) and external triggers (e.g., over-urbanization and heavy rain falls).

Figure 5. (**a**) ALOS PALSAR-derived surface annual motion rates over Hong Kong using the SB-InSAR method; the black arrows indicate reclamation lands; the red and pink arrows indicate the satellite flight path and looking direction of line of sight, respectively; black rectangles "1-Disneyland, Lantau Island" and "2-Tai Lam, Yuen Long, New Territories" indicate the TerraSAR monitoring sub-regions. Black polygons indicate the original Lam Chau and Check Lap Kok Island; (**b**) SPOT 5 imagery indicates the land cover of Hong Kong.

5.2. TerraSAR

Stripmap TerraSAR-X (3 m ground resolution, 11 days revisit cycle) data were applied in this study. A 3 × 2 multi-looking in range and azimuth, and the Goldstein filter [46], were employed for differential interferogram generation in order to derive a ground resolution of 4 m; and two sub-regions extracted from the PALSAR result (marked by black rectangles in Figure 5) were further analyzed, including "1"—Disneyland, Lantau Island and "2"—Tai Lam, Yuen Long, New Territories.

Figure 6 illustrates the SB-InSAR derived surface motion rates over the Disneyland region, Lantau Island overlapped on the DEM-shaded imagery. The subset image (a) was spatially cropped from Figure 5, and (b) from the TerraSAR result. The movement values of TerraSAR were primarily in the range of −20 mm/yr to 5 mm/yr, where reclaimed regions were highlighted as suffering from severe subsidence (e.g., the second-phase reclaimed zone of Disneyland Park with annual rate as low as −30 mm/yr). The mountain regions demonstrated mild LOS uplift or subsidence. A drastically enhanced density of CPs was detected: 215,156 CPs in approximately 17 km^2 (12,656 CPs/km^2). It is evident that a portion of slopes over Disneyland region was unstable as shown by significant LOS values (larger than ±2 mm/yr) both from ALOS PALSAR and TerraSAR-X results (Figure 6).

Figure 6. SB-InSAR derived LOS surface annual motion rates over Disneyland region superimposed on the DEM-shade imagery. The black cross indicates the location of a coherent pixel (CP) for time series comparison shown in Section 5.3, the red and pink arrows indicate the satellite flight path and looking direction of line of sight, respectively; (**a**) PALSAR for the observation period from June 2007 to January 2011; (**b**) TerraSAR for the observation period from October 2008 to December 2010.
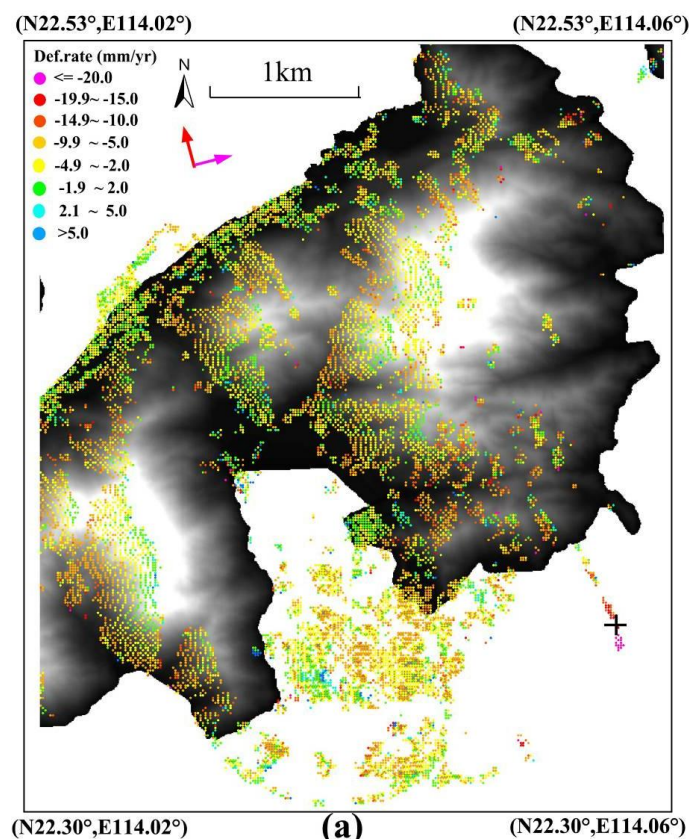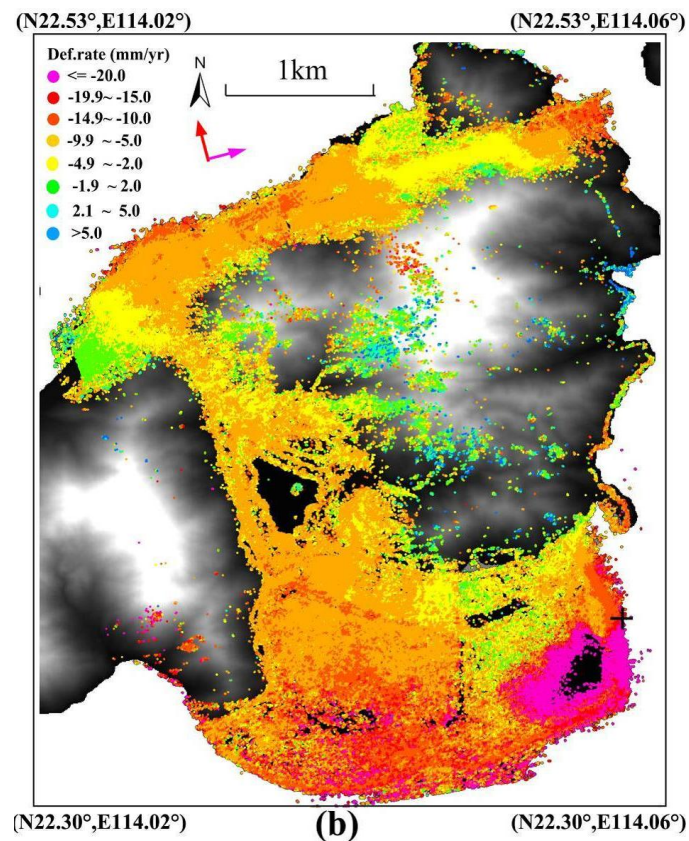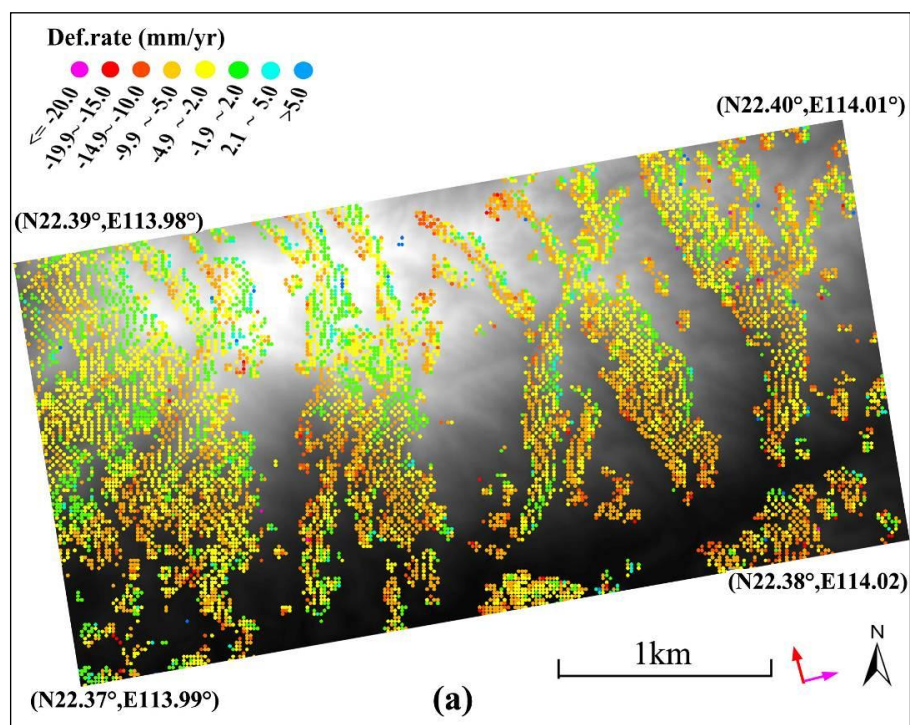
Figure 6. *Cont.*

Figure 7. SB-InSAR derived LOS surface annual motion rates over Tai Lam region, the red and pink arrows indicate the satellite flight path and looking direction of line of sight, respectively. (**a**) PALSAR for the observation period from June 2007 to January 2011; (**b**) TerraSAR-X for the observation period from October 2008 to December 2010.
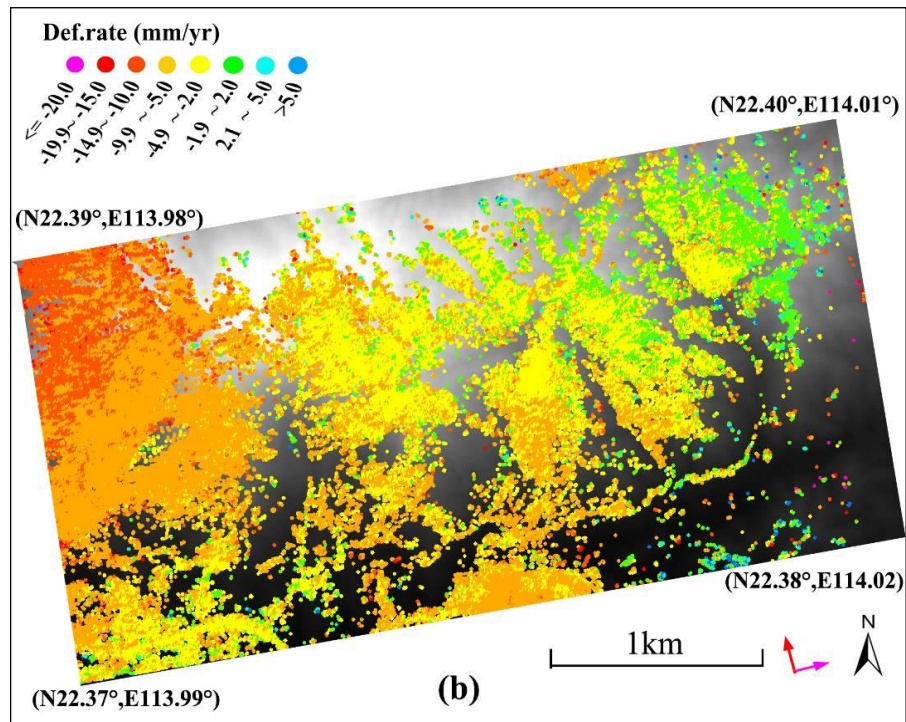
Figure 7. *Cont.*

(b)

Figure 7 illustrates the surface motion rates of (a) PALSAR and (b) TerraSAR-X over the sub-region "2"—Tai Lam, Yuen Long, New Territories, overlapped on the DEM-shaded imagery as well. It is clear that significant superficial displacements were evident over mountainous regions, implying the occurrence of unstable slopes because of the heavily weathered mantles, sparse vegetation as well as intense rainfall erosion during rainy seasons. Similar to the sub-region "1", the density of CPs extracted from TerraSAR-X has been drastically enhanced, *i.e.*, 93,367 CPs in approximately 11 km^2 (8,487 CPs/km^2).

5.3. Cross Comparison and Interpretation

In order to properly assess the potentials of the use of both PALSAR and TerraSAR-X data, three different factors, including wavelength, spatial resolution and revisit time, were analyzed. Then, a cross comparison of the SB-InSAR results between L- and X-band was undertaken as an additional quantitative validation. Finally, the performances of L- and X-band sensing were compared in detail with regard to aspects of slope, acquisition geometry and vegetation.

Interferometric phase decorrelation is fully influenced by wavelength, spatial resolution and revisit time according to the surface cover, which determines the backscattering characteristics. In general, compared to X-band TerraSAR (wavelength of 3.0 cm), L-band PALSAR guarantees better coherence over vegetated area due to its long wavelength (23.6 cm). The main advantages of TerraSAR include higher resolution and more frequent revisits providing spatial resolution 5–6 times better and revisit cycle 4–5 times shorter than ALOS PALSAR. The more frequent revisits of the present X-band missions counterbalances the possible negative effect of the shorter wavelength on temporal analysis in the presence of high rate displacements as well as substantial time series improvement [47]. Due to the above advantages, the spatial density of detected CPs has been increased, particularly over bare land.

The CPs of TerraSAR in the Disneyland, Lantau Island (as illustrated in Figure 6) was 215,156, nearly 20 times more than 11,255 of PALSAR for the same area. For the Tai Lam, New Territories, the number of CPs was 93,367 for TerraSAR, approximately 10 times greater than 10,833 of PALSAR. The latter figure was less than the former owing to a larger proportion of vegetation occurrence in Tai Lam study site.

As illustrated in Figures 6 and 7, the SB-InSAR derived LOS motion patterns from PALSAR and TerraSAR datasets were approximately consistent with values primarily in the range of −20 mm/yr to 5 mm/yr. In order to minimize the errors from residual topography and stratification component of atmospheric phase screen (APS), motion time series of a CP (with uniform geo-coordinates) from PALSAR and TerraSAR in the second-phase reclaimed zone of Disneyland Park were first compared, as illustrated in Figure 8a. Thanks to the more frequent revisits, more detailed time series of the CP (marked by the black cross in Figure 6) can be derived using TerraSAR data. The motion discrepancy of those two data showed a good agreement; and their absolute differences were calculated, varying from 1 to 5 mm with an average of 2.34 mm and standard deviation of 4.16 mm. Then, the annual displacement rates measured by PALSAR and TerraSAR-X on coincident CPs (with uniform geo-coordinates) in Disneyland region of Lantau Island (Figure 7) were compared. The scatter plot in Figure 8b showed consistent motion trend, represented by the linear fitting function y = 1.08 × −0.47 (R^2 = 0.726) and the dispersion value 7 mm/yr (within the [−2σ, +2σ] confidence test). The dispersion of motion rates between PALSAR and TerraSAR can be interpreted in three aspects: first, the observation spans (PALSAR, June 2007 to January 2011 *vs.* TerraSAR, October 2008 to December 2010) of the two datasets were different; second, the atmospheric artifacts of X-band TerraSAR were more severe than that of L-band PALSAR, introducing more errors in the motion estimation using SB-InSAR, particularly in mountainous regions; third, the spatial resolution of L- and X-band data were different (16 × 16 m^2 of PALSAR *vs.* 4 × 4 m^2 of TerraSAR), capturing different movements averaged on a pixel with different spatial extent.

Figure 8. Quantitative validation by means of the cross comparison between ALOS PALSAR and TerraSAR; (**a**) time series at the point marked by the black cross in Figure 6; (**b**) the scatter plot of annual displacement rates from coincident CPs in Figure 6 (the point in (a) indicated by the red ellipse).
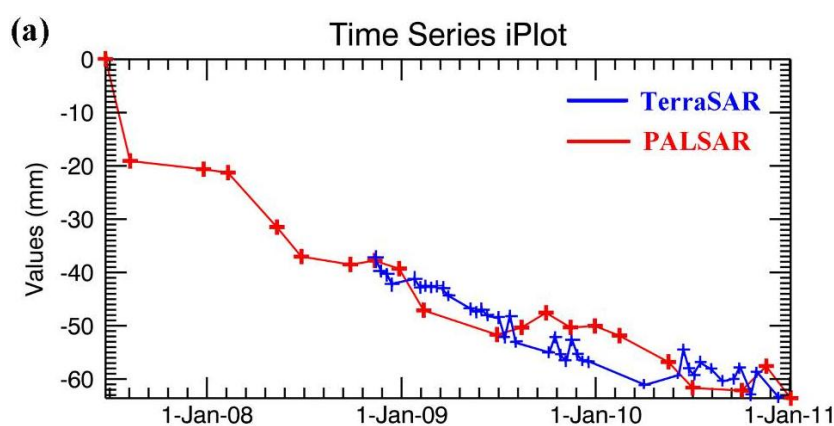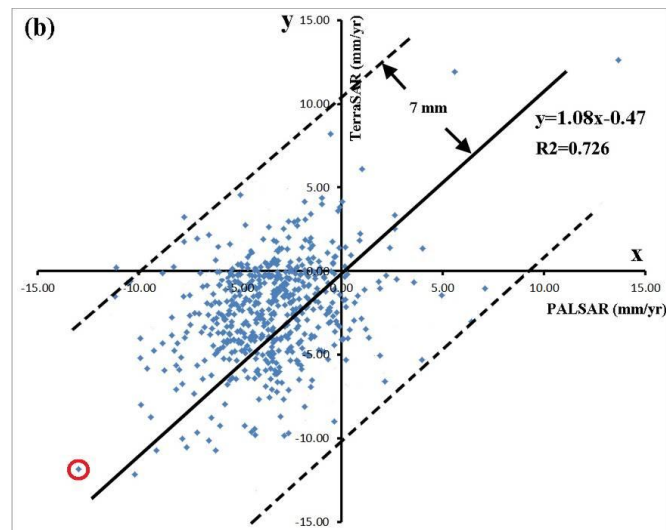
Figure 8. *Cont.*

In order to exclude other possible deformation causes (e.g., reclaimed land settlement); a slope map over the Disneyland region was generated using DEM data. Local variations in slope and gradient make InSAR LOS values hard to interpret in Hong Kong. However, if the assumption of progressive flattening movement holds, according to the geometric relationship between SAR imaging and downward slope surface motions (Figure 4), velocity values along the maximum slope direction can be calculated with the assistance of high-resolution DEM data. Then, the superficial displacement devoted to slope (projected along the maximum slope) was derived using a slope angle threshold (10 degrees), as illustrated in Figure 9. Figure 9a,b indicate the motion rates of PALSAR and TerraSAR-X, respectively, overlapped on the slope map. Owing to the higher movement sensitivity and spatial resolution, unstable slopes can be more easily discriminated in the TerraSAR-X result than in that of PALSAR. Unstable slopes, marked by black polygons were identified in Figure 9b according to the distinct boundary of moving to non-moving targets. Figure 9c,d show the unfavorable slopes (layovers and shadows) calculated by the sensor acquisition geometry and DEM in Disneyland region, demonstrating comparable results caused by the same flight path (ascending) and consistent radar look angles (34.3 ° of PALSAR and 37.4 ° of TerraSAR-X). Referring to the land cover of high-resolution imagery from Google Earth as shown in Figure 9e, it is clear that the distribution of CPs on PALSAR is almost even irrespective of whether the observed scenario is vegetated or not. The absence of CPs of PALSAR was primarily due to unfavorable slopes (layover/shadows, as illustrated in Figure 9c) or smooth backslopes (the transmitted radar signature cannot scatter or reflect back to the sensor receiver). Note that unlike persistent scatters, CPs exist on layover regions in this study but at a very low frequency (as marked by black arrows in Figure 9). This phenomenon can be explained from two opposite aspects: first, the scattering characteristic of features is homogeneous in the marked layover region, resulting in high-coherent CPs in the spatial-temporal domain; on the other hand, the occurrence of CPs in the layover is artifacts, requiring further removal. With regard to the TerraSAR-X result, CPs concentrate on exposed surfaces, e.g., artificial features and bare rocks. That is, 90% more CPs in exposed surfaces *versus* 10% in sparse vegetation areas (for dense vegetated area, no CP is extracted due to the total decorrelation of TerraSAR-X). Similar to PALSAR, the absence of CPs of TerraSAR-X was also be jointly influenced by the shadows (Figure 9d) and smooth backslopes.

Figure 9. Performance evaluation of ALOS PALSAR and TerraSAR for the unstable slope monitoring, black arrows indicate the occurrence of CPs on layovers in this study; (**a**) PALSAR-derived slope-projected data; and (**b**) TerraSAR-derived slope-projected data overlapped on the slope map of Disneyland region (suspected unstable slopes marked by black polygons); (**c**) and (**d**) are visibility maps of PALSAR, TerraSAR indicating layovers and shadows; (**e**) high resolution optical imagery from Google Earth (GE) shows the vegetation coverage and exposed surface.
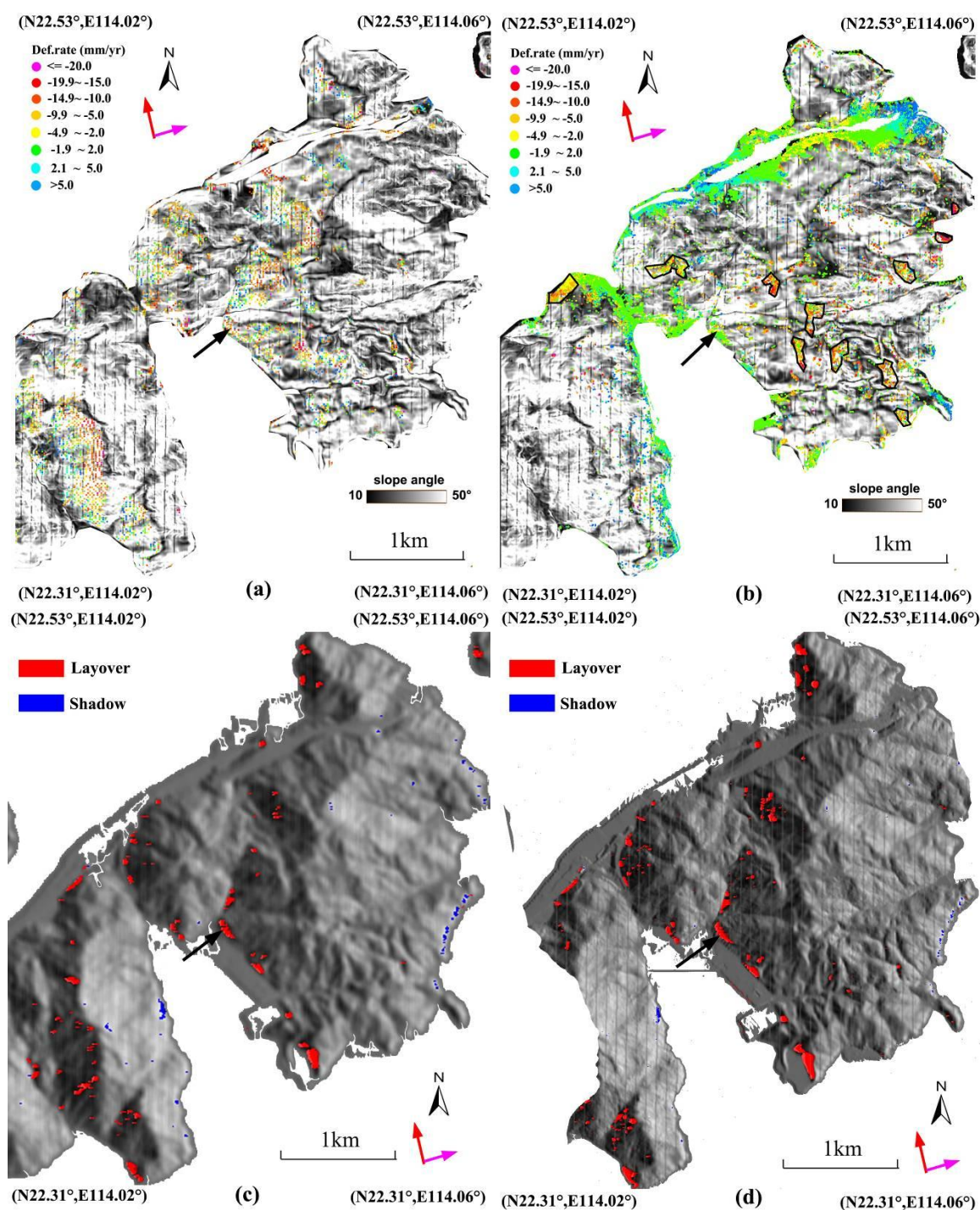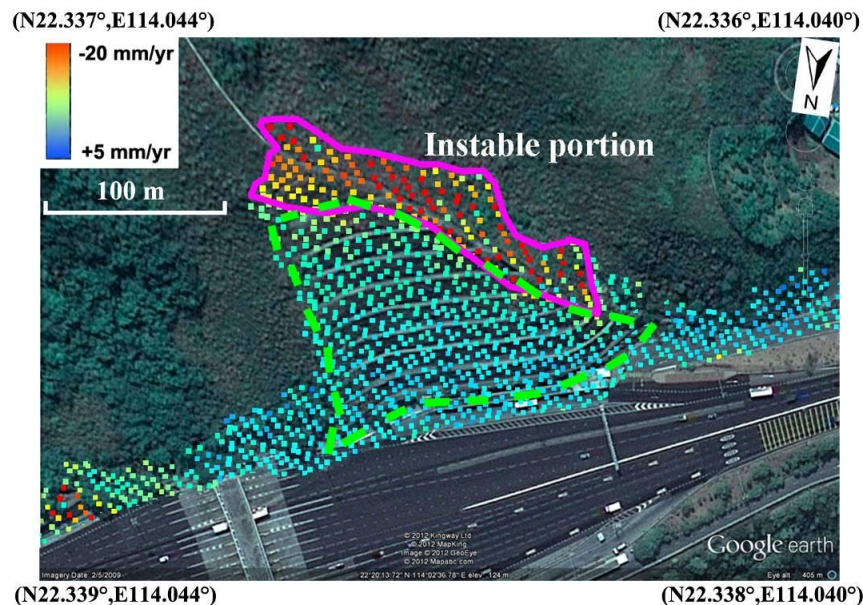
Figure 9. *Cont.*

6. Effects of Slope Consolidation in the Lantau Island

This Island has a rugged terrain composed of volcanic rocks in the west and intrusive granite rocks in the northeast. These two rock types have been severely weathered *in situ*, resulting in occurrence of slope instability over colluvium deposits or loose covering layers triggered by heavy rainfall. Figure 10 illustrates slope-projected motion rates of a consolidated slope nearby the Lantau Highway. It is clear that unstable slope boundaries can be distinguished (marked by the pink polygon) from its surrounding features due to the high spatial density of TerraSAR-X measurements. The consolidation was conducted around 2005–2006. After the countermeasure, the reinforced portion (marked by the green polygon) revealed stability with motion values ranging from −2 mm/yr to 2 mm/yr; in contrast, the upper portion (marked by the pink polygon) without reinforcement revealed instability demonstrating evident motion values (−20 mm/yr to −5 mm/yr). This phenomenon shows the effectiveness and importance of preventative measures, particularly in vulnerable locations along man-made infrastructures, to avoid potential geo-hazards.

Figure 10. Slope-projected motion rates of a consolidated slope nearby the Lantau Highway in a hot-spot of Disneyland, which is superimposed on the Google Earth (GE) image. Unstable surface (within the boundary marked by the pink polygon) still exists nearby the consolidated one, showing the effectiveness and importance of preventive measures (marked by the green polygon).

7. Conclusions

Regarding the observed scenarios, a majority of landslides (approximately 90%) in Hong Kong occurred on slopes with gradients less than 60°, and thus have been covered by the range of current SAR incidences to minimize unfavorable slopes (layover and shadow). Multi-source SAR data with different spatial resolutions, swath coverage, wavelengths and revisit times provide us a synthetic observation solution for slope superficial displacement surveillance. In this paper, the L-band ALOS PALSAR data were used for large-scale natural scenarios monitoring owing to its width swath and high coherence preservation in vegetated areas. High resolution TerraSAR data with shorter revisit times were beneficial for detailed information extraction, e.g., unstable slope boundary identification. Consequently, the advantages of the two different SAR systems can be integrated, providing crucial clues (e.g., motion inhomogeneity) that are important for early warning on geo-hazards. Generally, MT-InSAR approaches are promising for vulnerable slopes monitoring by means of detectable displacements on post-failures and landslide reactivations, even in the absence of in-situ controls. However, two key issues need attention. First, only bare or sparse vegetated slopes with mild-median slope gradients can be measured except for facing slopes covered by buildings or outcrops. Densely vegetated scenarios introduce severe temporal decorrelation even within hours, hampering the detection of PSs or DSs (no or sparse points were extracted); cliff slopes generate layovers on the facing direction and shadows on the other side because of the radar "ranging" mechanism (see Figure 9c,d); Second, MT-InSAR methods only measure the superficial LOS displacement of Extremely Slow (ES, velocity < 16 mm/yr) and Very Slow (VS, 16 mm/yr ≤ velocity < 1.6 m/yr) slopes [1,25,26] (Figures 5–7,9), limiting the usefulness of the technology for other landslide categories. Under the

assumption of progressive flattening movement, the maximum-slope projected movements found in this study (Figures 9 and 10) contribute towards an improved understanding of slope physical processes in the spatial-temporal domain. However, once different acquisition geometries are available, such as paired ascending and descending datasets over the same scene, a full 3-D deformation field might be reconstructed [48–50].

The main conclusions of this work can be summarized as follows:

(1) Rapid urban development in hilly terrain, coupled with tropical rainy storms and weathered covering rocks, has led to the frequent occurrence of disastrous landslides in Hong Kong. Most of those failures are minor and shallow in depth with a volume of usually less than 50 m^3 [37] and occurred in vegetated region. Although challenging, the synergistic analysis of L-band PALSAR and X-band TerraSAR provides a feasible solution for taking advantage of high resolution, frequent revisit times as well as long wavelength for the monitoring of superficial displacement of ES and VS slopes. The experimental results imply that SB-InSAR is potential for unstable slope surveillance due to the introduction of 3-D phase unwrapping coupled with the occurrence of DSs in the natural scenario of Hong Kong, e.g., 376 CPs/km^2 of L-band PALSAR covering the whole Hong Kong area, 12,656 and 8,487 CPs/km^2 of X-band TerraSAR in the Disneyland and Tai Lam sub-regions, respectively.

(2) In case of monitoring superficial displacement of slopes, application of currently available spaceborne SAR systems are feasible (approximately 90% landslides occurred in areas with gradients less than 60°) in Hong Kong owing to the wide incidence coverage (20°–60°), minimizing the occurrence of layovers and shadows. The phenomena of slope superficial movements are exploited by the SB-InSAR technique applied in this study. A quantitative comparison between L- and X-band dataset was undertaken. The results demonstrated that: X-band TerraSAR is more seriously affected by the vegetation (only 10% of CPs extracted in sparse vegetated regions) in comparison to an almost even spatial distribution of CPs of L-band PALSAR over the same observed scenario. Second, X-band TerraSAR is more capable of identifying unstable slopes (see Figures 9 and 10) owing to the higher sensitivity to movements as well as spatial resolution. Consequently, we suggest that the two different spaceborne SAR data need to be integrated for the improvement in the performance of monitoring unstable slope movements.

Acknowledgments

Author Contributions

Fulong Chen did the multi-temporal InSAR data processing, and inverted InSAR measurements to surface and slope-projected motions. He together with Hui Lin and Xianzhi Hu collected the precise

leveling data, and then for the InSAR-derived results validation and interpretation. All the authors contributed to developing the ideas presented and the writing of the paper.

Conflicts of Interest

The authors declare no conflict of interest.

References

1. Cruden, D.M.; Varnes, D.J. Special Report 247. Landslide Types and Processes. In *Landslides: Investigation and Mitigation*; Turner, A.K., Schuster, R.L., Eds.; National Academy Press: Washington, DC, USA, 1996; pp. 36–75.
2. Guzzetti, F.; Mondini, A.C.; Cardinali, M.; Fiorucci, F.; Santangelo, M.; Chang, K.-T. Landslide inventory maps: New tools for an old problem. *Earth Sci. Rev.* **2012**, *112*, 42–66.
3. Westen, C.J.; Castellanos, E.; Kuriakose, S. Spatial data for landslide susceptibility, hazard, and vulnerability assessment: An overview. *Eng. Geol.* **2008**, *102*, 112–131.
4. Strozzi, T.; Ambrosi, C.; Raetzo, H. Interpretation of aerial photographs and satellite SAR interferometry for the inventory of landslides. *Remote Sens.* **2013**, *5*, 2554–2570.
5. Qiao, G.; Lu, P.; Scainoni, M.; Xu, S.; Tong, X.; Feng, T.; Wu, H.; Chen, W.; Tian, Y.; Wang, W.; *et al.* Landslide investigation with remote sensing and sensor network: From susceptibility mapping and scaled-down simulation towards *in situ* sensor network design. *Remote Sens.* **2013**, *5*, 4319–4346.
6. Singhroy, V.; Molch, K. Characterizing and monitoring rockslides from SAR techniques. *Adv. Space Res.* **2004**, *33*, 290–295.
7. Li, Z.; Fielding, E.J.; Cross, P. Integration of InSAR time series analysis and water vapour correction for mapping postseismic deformation after the 2003 Bam, Iran Earthquake. *IEEE Trans. Geosci. Remote Sens.* **2009**, *47*, 3220–3230.
8. Zebker, H.A.; Rosen, P.A.; Goldstein, R.M.; Gabriel, A.; Werner, C.L. On the derivation of coseismic displacement fields using differential radar interferometry: The Landers earthquake. *J. Geophys. Res.* **1994**, *99*, 19617–19634.
9. Lu, Z.; Dzurisin, D.; Biggs, J.; Wicks, C., Jr.; McNutt, S. Ground surface deformation patterns, magma supply, and magma storage at Okmok volcano, Alaska, inferred from InSAR analysis: I. Inter-eruptive deformation, 1997–2008. *J. Geophys. Res.* **2010**, *115*, doi:10.1029/2009JB006969.
10. Luckman, A.; Quincey, D.; Bevan, S. The potential of satellite radar interferometry and feature tracking for monitoring flow rates of Himalayan glaciers. *Remote Sens. Environ.* **2007**, *111*, 172–181.
11. Chen, F.; Lin, H. Multi-baseline differential SAR interferometry analysis of Lantau Highway, Hong Kong, using ENVIsat ASAR data. *Remote Sens. Lett.* **2011**, *2*, 167–173.
12. Lin, H.; Chen, F.; Zhao, Q. Land deformation monitoring using coherent target-neighborhood networking method combined with polarimetric information—A case study of Shanghai, China. *Int. J. Remote Sens.* **2011**, *32*, 2395–2407.
13. Ferretti, A.; Prati, C.; Rocca, F. Nonlinear subsidence rate estimation using persistent scatterers indifferential SAR interferometry. *IEEE Trans. Geosci. Remote Sens.* **2000**, *38*, 2202–2212.

14. Hooper, A.; Zebker, H.; Segall, P.; Kampes, B. A new method for measuring deformation on volcanoes and other natural terrains using InSAR persitent scatterers. *Geophys. Res. Lett.* **2004**, *31*, doi:10.1029/2004GL021737.

15. Werner, C.; Wegmuller, U.; Strozzi, T.; Wiesmann, A. Interferometric Point Target Analysis for Deformation Mapping. In Proceedings of the IEEE Geoscience and Remote Sensing Symposium (IGARSS'03), Toulouse, France, 21–25 July 2003.

16. Berardino, P.; Fornaro, G.; Lanari, R.; Sansosti, E. A new algorithm for surface deforamtion monitoring based on small baseline differential SAR interferograms. *IEEE Trans. Geosci. Remote Sens.* **2002**, *40*, 2375–2383.

17. Chen, F.; Lin, H.; Zhang, Y.; Lu, Z. Ground subsidence geo-hazards induced by rapid urbanization: Implications from InSAR observation and geological analysis. *Nat. Harzards Earth Syst. Sci.* **2012**, *12*, 935–942.

18. Lanari, R.; Mora, O.; Manunta, M. A small-baseline approach for investigating deformations on full-resolution differential SAR interferograms. *IEEE Trans. Geosci. Remote Sens.* **2004**, *42*, 1377–1386.

19. Li, Z.; Liu, Y.; Zhou, X.; Cross, P.; Feng, W. Using small baseline interferometric SAR to map nonlinear ground motion: A case study in northern Tibet. *J. Appl. Geod.* **2009**, *3*, 163–170.

20. Ferretti, A.; Fumagalli, A.; Novali, F.; Prati, C.; Rocca, F.; Rucci, A. A new algorithm for processing interferometric data-stacks: SqueeSAR. *IEEE Trans. Geosci. Remote Sens.* **2011**, *49*, 3460–3470.

21. Hooper, A. A multi-temporal InSAR method incorporating both persistent scatterer and small baseline approaches. *Geophys. Res. Lett.* **2008**, *35*, 1–5.

22. Cascini, L.; Fornaro, G.; Peduto, D. Analysis at medium scale of low-resolution DInSAR data in slow-moving landslide-affected areas. *ISPRS J. Photogramm. Remote Sens.* **2009**, *64*, 598–611.

23. Cascini, L.; Fornaro, G.; Peduto, D. Advanced low- and full-resolution DInSAR map generation for slow-moving landslide analysis at different scales. *Eng. Geol.* **2010**, *112*, 29–42.

24. Cigna, F.; Ventisette, C.D.; Liguori, V.; Casagli, N. Advanced radar-interpretation of InSAR time series for mapping and characterization of geological processes. *Nat. Hazard. Earth Syst. Sci.* **2011**, *11*, 865–881.

25. Cigna, F.; Bianchini, S.; Casagli, N. How to assess landslide activity and intensity with Persistent Scatterer Interferometry (PSI): The PSI-based matrix approach. *Landslides* **2012**, *10*, 267–283.

26. Colesanti, C.; Wasowski, J. Investigating landslides with space-borne synthetic aperture radar (SAR) interferometry. *Eng. Geol.* **2006**, *88*, 173–199.

27. Farina, P.; Colombo, D.; Fumagalli, A.; Marks, F.; Moretti, S. Permanent scatterers for landslide investigations: Outcomes from the ESA-SLAM project. *Eng. Geol.* **2006**, *88*, 200–217.

28. Guzzetti, F.; Manunta, M.; Ardizzone, F.; Pepe, A.; Cardinali, M.; Zeni, G.; Reichenbach, P.; Lanari, R. Analysis of ground deformation detected using the SBAS-DInSAR technique in Umbria, Central Italy. *Pure Appl. Geophys.* **2009**, *166*, 1425–1459.

29. Lauknes, T.R.; Shanker, A.P.; Dehls, J.F.; Zebker, H.A.; Henderson, I.H.C.; Larsen, Y. Detailed rockslide mapping in northern Norway with small baseline and persistent scatterer interferometric SAR time series methods. *Remote Sens. Environ.* **2010**, 114, 2097–2109.

30. Strozzi, T.; Farina, P.; Corsini, A.; Ambrosi, C.; Thüring, M.; Zilger, J.; Wiesmann, A.; Wegmüller, U.; Werner, C. Survey and monitoring of landslide displacements by means of L-band satellite SAR interferometry. *Landslides* **2005**, *2*, 193–201.

31. Bianchini, S.; Cigna, F.; del Ventisette, C.; Moretti, S.; Casagli, N. Detecting and Monitoring Landslide Phenomena with TerraSAR-X Persistent Scatterers Data: The Gimigliano Case Study in Calabria Region (Italy). In Proceedings of the 2012 IEEE International Geoscience and Remote Sensing Symposium (IGARSS'12), Munich, Germany, 22–27 July 2012; Volume 6351237, pp. 982–985.

32. Bovenga, F.; Wasowski, J.; Nitti, D.O.; Nutricato, R.; Chiaradia, M.T. Using COSMO/SkyMed X-band and ENVISAT C-band SAR interferometry for landslides analysis. *Remote Sens. Environ.* **2012**, *119*, 272–285.

33. Chen, F.; Lin, H.; Yeung, K.; Cheng, S. Detection of slope instability in Hong Kong based on multi-baseline differential SAR interferometry using ALOS PALSAR data. *GISci. Remote Sens.* **2010**, *47*, 208–220.

34. Zhou, C.H.; Lee, C.F.; Li, J.; Xu, Z.W. On the spatial relationship between landslides and causative factors on Lantau Island, Hong Kong. *Geomorphology* **2002**, *43*, 197–207.

35. Parry, S. The application of geomorphological mapping in the assessment of landslide hazard in Hong Kong. *Dev. Earth Surf. Process.* **2011**, *15*, 413–441.

36. Evans, N.C.; King, J.P. *Natural Terrain Landslide Study Debris Avalanches Susceptibility, Hong Kong*; Technical Note TN 1/98; Geotechnical Engineering Office: Hong Kong, China, 1998; p. 96.

37. Chen, H.; Lee, C.F. Geohazards of slope mass movement and its prevention in Hong Kong. *Eng. Geol.* **2004**, *76*, 3–25.

38. Hanssen, R.F. *Radar Interferometry: Data Interpretation & Error Analysis*; Kluwer Academic Publishers: Dordrecht, The Netherlands, 2001; p. 138.

39. Nitti, D.O.; Hanssen, R.F.; Refice, A.; Bovenga, F.; Nutricato, R. Impact of DEM-assisted coregistration on high-resolution SAR interferometry. *IEEE Trans. Geosci. Remote Sens.* **2011**, *49*, 1127–1143.

40. Costantini, M.; Rosen, P. A Generalized Phase Unwrapping Approach for Sparse Data. In Proceedings of the International Geoscience and Remote Sensing Symposium 1999 (IGARSS'99), Hamburg, Germany, 28 June–2 July 1999.

41. Costantini, M.; Malvarosa, F.; Minati, F. A general formulation for redundant integration of finite differences and phase unwrapping on a sparse multidimensional domain. *IEEE Trans. Geosci. Remote Sens.* **2012**, *50*, 758–768.

42. Hooper, A.; Zebker, H. Phase unwrapping in three dimensions with application to InSAR time series. *J. Opt. Soc. Am. A* **2007**, *24*, 2737–2747.

43. Shanker, P.; Zebker, H. Edgelist phase unwrapping algorithm for time series InSAR analysis. *J. Opt. Soc. Am.* **2010**, *27*, 605–612.

44. Pepe, A.; Lanari, R. On the extension of the miminum cost flow algorithm for phase unwrapping of multitemporal differential SAR interferograms. *IEEE Trans. Geosci. Remote Sens.* **2006**, *44*, 2374–2383.

45. Samsonov, S. Topographic correction for ALOS PALSAR interferometry. *IEEE Trans. Geosci. Remote Sens.* **2010**, *48*, 3020–3027.

46. Goldstein, R.M.; Werner, C.L. Radar interferogram filtering for geophysical applications. *Geophys. Res. Lett.* **1998**, *25*, 4035–4038.
47. Sansosti, E.; Casu, F.; Manzo, M.; Lanari, R. Space-borne radar interferometry techniques for the generation of deformation time series: An advanced tool for Earth's surface displacement analysis. *Geophys. Res. Lett.* **2010**, *37*, doi:10.1029/2010GL044379.
48. Rocca, F. 3D Motion Recovery with Multi-Angle and/or Left Right Interferometry. In Proceedings of the Third International Workshop on ERS SAR Interferometry (FRINGE 2003), Frascati, Italy, 2–5 December 2003.
49. Wright, T.J.; Parsons, B.E.; Lu, Z. Toward mapping surface deformation in three dimensions using InSAR. *Geophys. Res. Lett.* **2004**, *31*, doi:10.1029/2003GL018827.
50. Tofani, V.; Raspini, F.; Catani, F.; Casagli, N. Persistent Scatterer Interferometry (PSI) technique for landslide characterization and monitoring. *Remote Sens.* **2013**, *5*, 1045–1065.